



# Effect of different Na supply methods on thin Cu(In,Ga)Se<sub>2</sub> solar cells with Al<sub>2</sub>O<sub>3</sub> rear passivation layers



Dorothea Ledinek\*, Olivier Donzel-Gargand, Markus Sköld, Jan Keller, Marika Edoff

Uppsala University, The Ångström Laboratory, Department of Engineering Sciences, Postal Address: Box 534, 751 21 Uppsala, Sweden

## ARTICLE INFO

### Keywords:

Alkali  
Back contact  
CIGS  
Passivation  
Thin films  
Rear contact  
Tunneling

## ABSTRACT

In this work, rear-contact passivated Cu(In,Ga)Se<sub>2</sub> (CIGS) solar cells were fabricated without any intentional contact openings between the CIGS and Mo layers. The investigated samples were either Na free or one of two Na supply methods was used, i) a NaF precursor on top of the Al<sub>2</sub>O<sub>3</sub> rear passivation layer or ii) an in situ post-deposition treatment with NaF after co-evaporation of the CIGS layer. The thickness of the ALD-Al<sub>2</sub>O<sub>3</sub> passivation layer was also varied in order to find an optimal combination of Na supply and passivation layer thickness. Our results from electrical characterization show remarkably different solar cell behavior for different Na supplies. For up to 1 nm thick Al<sub>2</sub>O<sub>3</sub> layers an electronically good contact could be confirmed independently of Na deposition method and content. When the Al<sub>2</sub>O<sub>3</sub> thickness exceeded 1 nm, the current was blocked on all samples except on the samples with the NaF precursor. On these samples the current was not blocked up to an Al<sub>2</sub>O<sub>3</sub> layer thickness of about 6 nm, the maximum thickness we could achieve without the CIGS peeling off the Al<sub>2</sub>O<sub>3</sub> layer. Transmission electron microscopy reveals a porous passivation layer for the samples with a NaF precursor. An analysis of the dependence of the open circuit voltage on temperature (JVT) indicates that a thicker NaF precursor layer lowers the height of the hole barrier at the rear contact for the passivated cells. This energy barrier is also lower for the passivated sample, compared to an unpassivated sample, when both samples have been post-deposition treated.

## 1. Introduction

The record efficiency of Cu(In,Ga)Se<sub>2</sub> (CIGS) solar cells has tremendously increased over the last years due to improvements in the bulk quality and the front contact interface [1]. Just as in Si solar cell technology, the thickness of the absorber layer is expected to decrease for commercial CIGS solar cells to save costs and materials. Thus, controlling the recombination and maximizing the light reflection at the CIGS/rear contact interface will be of increasing importance for the solar cell performance.

Inspired by PERC (Passivated Emitter Rear Contact) silicon solar cells, Vermang et al. [2,3] introduced an Al<sub>2</sub>O<sub>3</sub> passivation layer between the CIGS absorber layer and the Mo rear contact. To ensure an electrical contact, different kinds of nano-contacts were developed: conducting Mo-nano-spheres embedded in the passivation layer [4] or nano-openings in the passivation layer [2,3]. Whereas thin (< 15 nm) passivation layers mostly increase the open-circuit voltage ( $V_{OC}$ ) by lowering the recombination rate at the rear contact [2], both, thicker Al<sub>2</sub>O<sub>3</sub> layers (30 nm) [3] and Mo nano-spheres [4], also increase the short-circuit current density ( $J_{SC}$ ) by increased reflection at the rear

contact and/or by phonons between Mo nano-spheres that enhance absorption. The higher  $V_{OC}$  has been explained by a field effect [5,6] (electrical passivation) due to negatively charged centers ( $V_{Al}$  and/or  $O_i$ ) in oxygen rich Al<sub>2</sub>O<sub>3</sub> layers [7], which lowers the interface recombination rate at the passivated areas. The electrical passivation effect increases strongly from 5 to 50 nm passivation layer thickness. The interface defect density, however, is found to only be slightly reduced compared to an unpassivated area [7].

The rear contact has been associated with a kink and roll-over in current-voltage ( $JV$ ) curves of CIGS solar cells measured especially at low temperatures [8–17]. The kink has been explained by a hole extraction barrier [10], whereas the roll-over has been explained by a hole injection barrier [8,10,12]. Some studies identified the valence band off-set between CIGS and MoSe<sub>2</sub>, that is usually formed between the CIGS and Mo [10,17], as the hole injection barrier. Even a cross-over between the dark and light curve can be explained by a barrier at the rear contact as exemplified for CdTe solar cells [11,18]. However, in the case of CIGS solar cells a conduction band offset between the CIGS and CdS [8] or an acceptor rich layer [10] in the CIGS near the front interface can also explain a kink and cross-over in the  $JV$  curve.

\* Corresponding author.

E-mail address: [ledinekdorothea@yahoo.de](mailto:ledinekdorothea@yahoo.de) (D. Ledinek).

<https://doi.org/10.1016/j.solmat.2018.07.017>

Received 28 May 2018; Received in revised form 12 July 2018; Accepted 17 July 2018

Available online 08 August 2018

0927-0248/ © 2018 The Authors. Published by Elsevier B.V. This is an open access article under the CC BY-NC-ND license (<http://creativecommons.org/licenses/by-nc-nd/4.0/>).

The rear contact region is strongly affected by the presence of Na. Whereas the soda-lime glass substrate can act as a source of Na during the CIGS co-evaporation, Na can also be added in a thin NaF precursor layer onto the rear contact before CIGS evaporation (pre-deposition treatment, pre-DT) [19] or by evaporating NaF on top of the CIGS layer during an annealing step after its deposition (post-deposition treatment, post-DT) [9]. While there is a general agreement, that Na application or Na diffusion from the soda-lime glass enhances the electrical properties of the rear contact, the exact mechanism is unclear. For example, a roll-over measured on Na-free devices at room temperature can be reduced by a Na pre-DT [10,19]. Pre-deposited Na [19] or Na from the soda-lime glass [20,21] acts as a catalyst and promotes the formation of MoSe<sub>2</sub>, which in turn creates an ohmic contact according to references [17,20,21]. In contrast, Yoon et al. [22] doubt that the MoSe<sub>2</sub> layer is the origin of the ohmic nature of the rear contact and suggest that Na reduces the barrier at the CIGS/MoSe<sub>2</sub> interface as it increases the (effective) doping of the CIGS or the MoSe<sub>2</sub> layer. Jarzembowski et al. [23] found that the rear interface recombination rate for samples with an alkali diffusion barrier is lowered by NaF post-DT. They concluded that Na passivates either the MoSe<sub>2</sub>/CIGS interface or the MoSe<sub>2</sub>/Mo interface.

In their first work on CIGS rear surface passivation, Vermang et al. [3] observed that the *JV* curves of solar cells with a 5 nm Al<sub>2</sub>O<sub>3</sub> passivation layer with point contact openings and without adding NaF, exhibited a kink and a roll-over. Insufficient Na from the soda-lime glass was suspected and a NaF precursor layer was successfully applied on the Al<sub>2</sub>O<sub>3</sub> layer before CIGS evaporation. The passivation layer without openings inhibited the electrical contact for the samples without the NaF treatment. This is in agreement with measurements on Al<sub>2</sub>O<sub>3</sub> on Mo with an Hg probe [24]. The sheet resistance as measured with the Hg probe was shown to be negligible for a passivation layer thinner than 3 nm. While direct tunneling dominates for low voltages and thin Al<sub>2</sub>O<sub>3</sub> layers (< 3 nm), Fowler-Nordheim tunneling dominates at voltages that are only reached at the rear contact for high forward biases much larger than *V*<sub>OC</sub> and thicker Al<sub>2</sub>O<sub>3</sub> layers. Vermang et al. [3] did not provide any *JV* curves for samples without nano-contacts but with NaF pre-deposition.

In this work, a series of passivated and unpassivated CIGS solar cells was produced. In order to evaluate if thin unpatterned passivation layers can provide a sufficiently strong passivation effect without blocking the current, no point contacts were etched into the passivation layers. Considering the significance of Na outlined above, the Na supply method and the Na concentration were varied in four ways (compare

**Table 1**

Overview of the produced samples. In column three, the first number gives the number of samples produced for every sample type and the numbers in brackets give the number of cells on every sample. The numbers in the fourth column indicates the corresponding number of ALD cycles. The number of ALD cycles replaces xx in the sample name (e.g. 'post-DT10' is a post-deposition treated sample passivated with a passivation layer deposited by 10 ALD cycles).

| Sample type           | Sample name | Number of samples (number of cells) | Number of ALD cycles for Al <sub>2</sub> O <sub>3</sub> xx |
|-----------------------|-------------|-------------------------------------|--|
| Post-Deposition       | post-DTxx   | 8 (32, 32, 32, 32, 32, 32, 32, 32)  | 0, 0, 10, 10, 20, 30, 50, 70                               |
| 7.5 nm pre-Deposition | 7.5pre-DTxx | 2 (32, 32)                          | 20, 50   |
| 15 nm pre-Deposition  | 15pre-DTxx  | 7 (32, 12, 12, 32, 32, 32, 32)      | 0, 10, 20, 30, 30, 50, 70                                  |
| Diffusion barrier     | barrierxx   | 3 (32, 32, 32)                      | 0, 10, 20  |
| Baseline              | baselinexx  | 1 (32)                              | 0  |

Fig. 1): i) NaF post-DT, ii) NaF pre-DT, iii) Na supply inhibited by a alkaline diffusion barrier and neither NaF pre-DT nor post-DT and iv) Na supply exclusively from the soda-lime glass substrate (labeled as “baseline”). The passivation layer thickness was varied to optimize it for the different Na supply methods. Current-voltage (*JV*) measurements at a wide range of temperatures were used to further characterize the rear contact for some combinations of passivation layer thickness and Na supply method.

## 2. Sample processing and characterization

An overview over the whole matrix of samples produced and sample names can be found in Table 1 and the different sample types are further illustrated in Fig. 1. Generally, the samples were produced according to our group's baseline process [25]. The cell area was scribed mechanically to an area of 0.5 cm<sup>2</sup> and every sample consists of 32 individual cells, except for two samples with 12 cells. In contrast to the baseline process described in reference [25] the co-evaporated CIGS layers were grown with constant evaporation rates, resulting in a flat [Ga]/([Ga] + [In]) ratio throughout the film, i.e. without a built-in electron barrier at the rear of the absorber layer. The Al<sub>2</sub>O<sub>3</sub> diffusion barriers, Al<sub>2</sub>O<sub>3</sub> passivation layers and NaF post- or pre-DT were added to the baseline process in the following way: For samples with a diffusion barrier, 300 cycles Al<sub>2</sub>O<sub>3</sub> were deposited directly on the cleaned

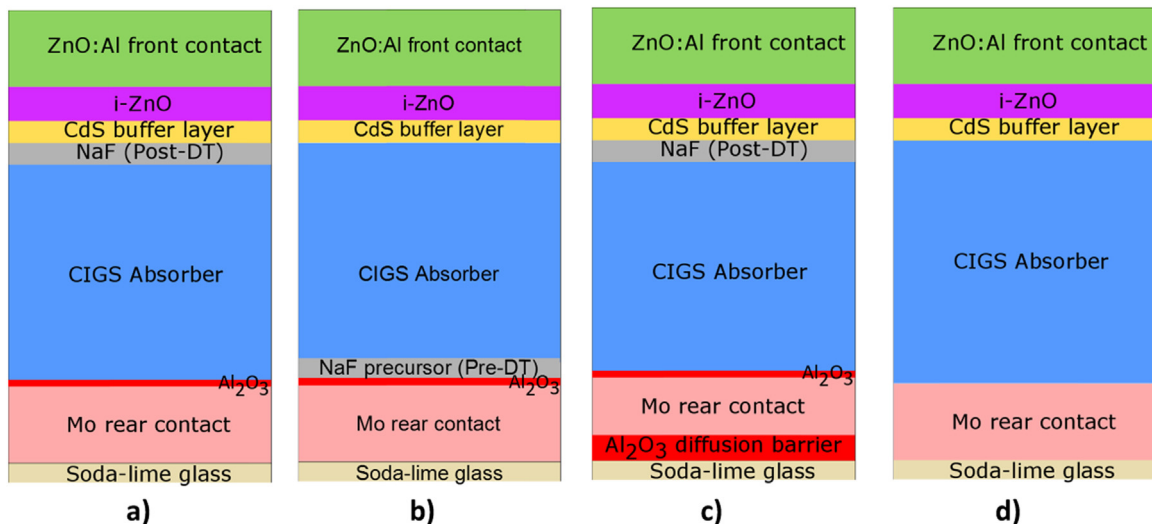


**Fig. 1.** Schematic representation of the different sample types: a) NaF post-deposition treated (post-DT) b) NaF pre-deposition treated (pre-DT), c) barrier, d) baseline. The passivation layer is very thin compared to all other layers and is indicated as a red line on top of the Mo rear contact.

glass by atomic layer deposition at 300 °C using H<sub>2</sub>O and trimethylaluminum (TMA) as precursors and nitrogen as a purge gas. For all passivated samples Al<sub>2</sub>O<sub>3</sub> was deposited on top of the Mo by the same ALD process. The thickness of the Al<sub>2</sub>O<sub>3</sub> layer was determined for 10, 20, 30, 50, 70 and 300 cycles by spectroscopic ellipsometry with a Woollam VASE instrument. The wavelength was swept between 260 and 1700 nm and the angle of incidence was 60, 65 and 70 degrees. A linear regression gave a layer thickness of 0.9 Å per ALD cycle. 7.5 or 15 nm NaF precursor layers (thickness measured by a quartz crystal rate monitor calibrated by measurements with a Dektak 150 stylus profilometer) were evaporated onto the pre-DT samples prior to the CIGS deposition.

To obtain the desired CIGS composition, the Se source was temperature controlled and the other metal sources were controlled by a quadrupole mass spectrometer set to constant evaporation rates. The samples were mounted in a holder heated from behind by IR lamps. The sample holder temperature was raised during the first 100 s from room temperature to 410 °C and stayed there for 1500 s, while the shutter was still closed and the sources were heated up to reach the pre-defined rates. During the first 125 s after the shutter opened, the substrate temperature stayed at 410 °C and during the following 125 s the temperature was linearly raised to 530 °C. Then the temperature was kept constant until the end of the evaporation after 450 more seconds. This last evaporation phase was shortened or prolonged to vary the thickness of the evaporated layer. 450 s gave a nominal CIGS layer thickness of 1.0 µm. The samples that did not undergo a post-DT cooled down to below 60 °C before venting the chamber with nitrogen and proceeding with the deposition of the CdS buffer layer by chemical bath deposition (CBD). For the post-DT absorbers, the samples cooled down to 490 °C. Then, NaF was evaporated onto the CIGS and the temperature was maintained constant for 400 s. Selenium was provided in excess even during the NaF evaporation phase. Subsequently, these samples also cooled down to below 60 °C before venting and CdS deposition.

The average thicknesses, CGI [Cu]/([In] + [Ga]) and the GGI [Ga]/([In] + [Ga]) were determined by XRF measurements that had been calibrated by a standard sample with known composition and mechanical profilometer measurements. In each run, test pieces for XRF measurements were placed on either side of the samples, which were located in the middle of the substrate holder. Therefore the actual composition values for all samples lie within the span of CGI = 0.80–0.92 and GGI = 0.13–0.18. The absorber thickness was determined to 0.95 ± 0.03 µm. The CIGS absorber peeled off from Al<sub>2</sub>O<sub>3</sub> layers deposited by > 70 ALD cycles.

The *JV* curves were measured in the dark and under illumination by a halogen lamp using a four-point probe setup. The light intensity was calibrated with a Si solar cell to obtain a photon flux corresponding to 1000 W/m<sup>2</sup> at AM 1.5. The temperature during the measurements was set to 300 K by a temperature stage cooled by a Peltier element. For the samples with 32 cells the average *JV* parameters of the eight cells with the highest efficiencies was calculated. For the two samples with 12 cells, the average *JV* parameters of the three best cells were used. If more than one sample was produced for a cell stack, average *JV* parameters for the samples and globally averaged *JV* parameters for the cell stack were calculated. As the sample averages did not differ substantially, only the global averages will be shown. External quantum efficiencies (*EQE*) were measured on the four best cells per sample under ambient light. The *EQE* was used to determine an approximate band gap of the absorber, to ensure that differences in *V<sub>OC</sub>* and *J<sub>SC</sub>* do not stem from changes in the absorber composition. *EQE*<sup>2</sup> was plotted against the photon energy *E* and the curve linearly fitted for the low *E* part. The intercept of the fitted line with the *E*-axis gives the approximate band gap energy *E<sub>G</sub>*. The calculated band gaps for all samples lie between 1.04 and 1.07 eV meaning that differences in the *V<sub>OC</sub>* larger than 30 meV cannot be explained by differences in the band gap.

Temperature dependent *JV* measurements were performed in a home-built cryostat on one cell on selected samples. The photon flux

from a white light emitting diode (LED) was calibrated at 300 K to result in 100%, 10% and 1% of the *J<sub>SC</sub>* that was previously measured with the *JV* set-up at 300 K. The stage temperature varied between 150 and 330 K with temperature steps of 10 K. Additionally, capacitance-voltage (*CV*) curves were measured for four cells per sample and the net acceptor concentration (*N<sub>A</sub>*) was calculated from *CV* curves by applying the depletion approximation [26].

Transmission Electron Microscopy (TEM) and Electron Energy Loss Spectroscopy (EELS) data acquisition were performed using a Tecnai F30ST (FEI) with a Tridiem post filter (863, Gatan) and was operated at 300 kV accelerating voltage. The subsequent data analysis was done through DigitalMicrograph (GMS 2.32, Gatan). The TEM lamellae were prepared with the help of a Focused Ion Beam (FIB) Strata DB235 (FEI) by the in-situ lift-out technique [27]. To perform the final polishing step the Ga-based ion beam was set to 5 kV and 50 pA for the accelerating voltage and the beam current, respectively.

### 3. Theory - Hole barrier height at the rear contact and *JVT* measurements

Assuming that a barrier at the rear contact is responsible for the roll-over of *JV* curves mentioned in the introduction, these curves have been modelled by 1) a secondary (photo)diode in series with the main junction [11,12,16–18,28–30], if the two junctions do not interact, or 2) a phototransistor behavior [13,15], if the two junctions interact (see Fig. 2). In model 1 and 2, the voltage over the complete solar cell is split into the voltage over the primary photodiode and over the secondary diode, so that the primary diode is forward biased and the secondary diode is reverse biased for voltages higher than *V<sub>OC</sub>* over the complete solar cell. The secondary diode's saturation current *J<sub>0b</sub>* is determined by a pre-factor *J<sub>00b</sub>* and a Boltzmann factor  $e^{-\phi_b/kT}$ , with  $\phi_b$  being the height of a barrier for holes at the rear contact, i.e. the energy difference between the Fermi level in the CIGS and the valence band at the CIGS-rear contact interface. For sufficiently small  $\phi_b$  the reverse biased secondary diode does not limit the current and *V<sub>OC</sub>* at room temperature. For optically thin solar cells or solar cells with a long minority carrier diffusion length, a secondary photocurrent is additionally generated [31]. If a shunt conductance is added in parallel to the (photo) diode in model 1 [11,29], four current components can flow over the reversely-biased rear contact: the diode's saturation current, a breakdown current for reverse biases over the secondary diode higher than its breakdown voltage, the secondary photocurrent and the current over the secondary shunt. *J<sub>0b</sub>* and the photocurrent determine the *JV* point above *V<sub>OC</sub>*, where the *JV* curve becomes current limited, and the slope of the roll-over curve is determined by the value of the shunt conductance. If the shunt conductance at the rear contact equals or is larger than the lumped series resistance of the device, the slope of the

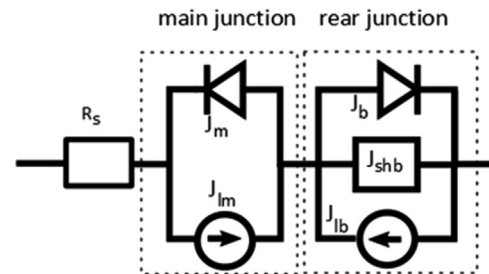


Fig. 2. Equivalent circuit of a two-diode model for thin film solar cells. The primary diode with a current source in parallel, represents the main junction and the associated currents, i.e. the diode current *J<sub>m</sub>* and the light current *J<sub>lm</sub>*, the secondary diode with a current source and a shunt in parallel represents an energy barrier at the rear contact and the associated currents: a diode current *J<sub>b</sub>*, a secondary light current *J<sub>lb</sub>* and a shunt current *J<sub>shb</sub>* = *G<sub>b</sub>* *V<sub>b</sub>*. The different series resistance components are combined together in a lumped series resistance *R<sub>s</sub>*.

roll-over matches the slope of the  $JV$  curve between the voltage at the maximum power point and  $V_{OC}$  and the roll-over disappears regardless of  $\phi_b$  [11]. The break-down of a reverse biased secondary diode increases the slope of the  $JV$  curves at high voltages drastically.  $\phi_b$  may be quantified by  $JVT$  measurements, either by extracting  $J_{ob}$  for model 1 for optically thick solar cells [16,17,30] or from  $V_{OC}$ - $T$  graphs for model 2 [13] and - as shown in the appendix- even for model 1 for optically thin solar cells. For model 1 the relationship between  $V_{OC}$  and  $T$  is linear for both low and high temperatures, but with different parameters. For low temperatures  $V_{OC} \approx \frac{E_a}{q} + \frac{A_m k T}{q} \ln \left( \frac{J_{lm}}{J_{00m}} \right)$  with the activation energy for the dominant recombination process  $E_a$ , the ideality factor for the main diode  $A_m$ , the light current generated at the main junction  $J_{lm}$  and the temperature dependent pre-factor of the saturation current of the main diode  $J_{00m}$ . For the low temperature region this equation becomes  $V_{OC} \approx \frac{E_a - \phi_b}{q} + \frac{k T}{q} \ln \left( \left( \frac{J_{lm}}{J_{00m}} \right)^{A_m} \left( \frac{J_{00b}}{J_{lb} - G_b \cdot V_{OCb}} \right)^{A_b} \right)$  with the temperature independent pre-factor of the saturation current  $J_{00b}$ , the ideality factor of the rear contact junction  $A_b$ , the light current generated at the rear contact  $J_{lb}$  and the current through the shunt at the rear junction  $J_{shb} = G_b V_{OCb}$ .  $\phi_b$  is thus the difference between the extrapolated  $V_{OCs}$  at 0 K.

## 4. Results

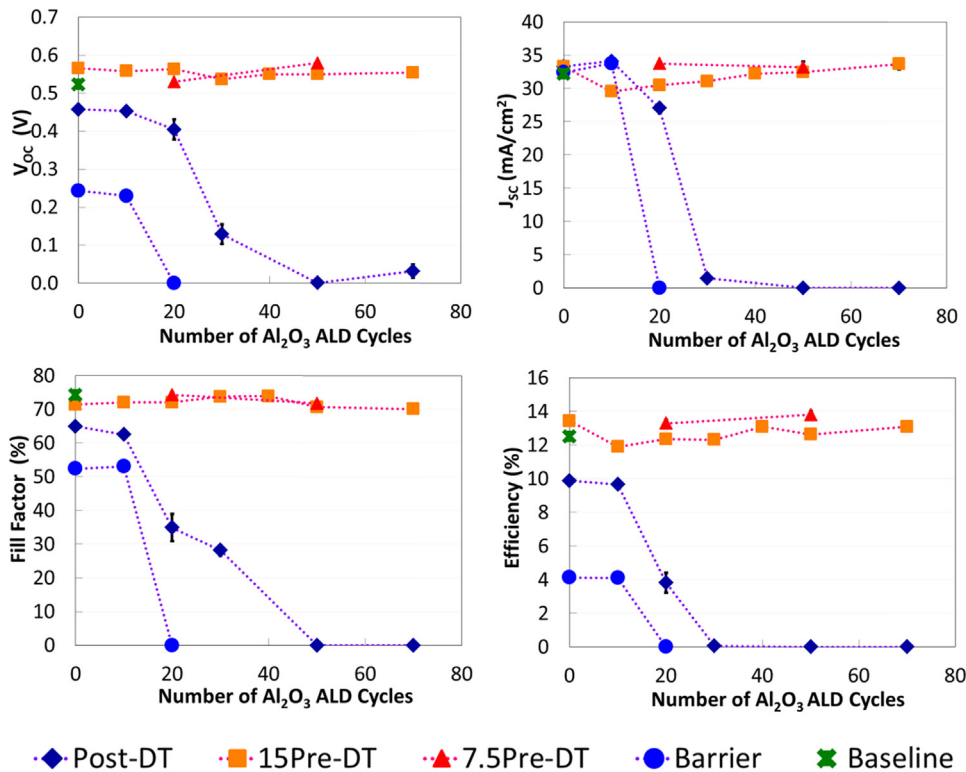
### 4.1. $JV$ and $EQE$ measurement

Fig. 3 summarizes the average photovoltaic parameters extracted from the  $JV$  measurements and illustrates the trends for increasing  $Al_2O_3$  thickness. For the post-DT samples and the barrier samples the passivation layer does not have a beneficial effect on the efficiency and it even has a detrimental effect for those samples with more than 10 ALD cycles. Whereas the  $J_{SC}$  increased for the post-DT10 and barrier10 samples compared to the corresponding samples without passivation, the  $V_{OC}$  is reduced for all passivation layer thicknesses. Passivation layers deposited by more than 10 ALD cycles block the current increasingly and the fill factor ( $FF$ ) deteriorates due to a kink in the  $JV$

curve. By contrast, no current blocking occurs when a NaF precursor layer is deposited on top of the  $Al_2O_3$  layer prior to the CIGS deposition. This is valid for both the 7.5pre-DT and 15pre-DT samples. These results clearly indicate that the rear contact properties of the passivated samples are essentially affected by the Na supply method. We will explore possible mechanisms in the discussion section, but first we present the  $JV$  and  $EQE$  data in more detail.

The following paragraphs illustrate the results of the  $JV$  and  $EQE$  measurement of a representative cell for selected constellations. For the post-DT samples (see Fig. 3 and Fig. 4), the cells with a  $Al_2O_3$  layer have lower or equal efficiencies compared to the unpassivated samples. Here, a 10 cycle passivation layer leads to a  $0.8 \text{ mA/cm}^2$  higher  $J_{SC}$ , but also to a reduced  $FF$  and  $V_{OC}$  as compared to the unpassivated case. The gain in  $J_{SC}$  stems from a higher  $EQE$  for medium and long wavelengths. The  $JV$  curve of the post-DT20 sample has a kink and all parameters are severely deteriorated. The  $JV$  curves of the samples with even thicker passivation layers block the photocurrent even more.

For the 15preDT samples the  $V_{OC}$  and the  $FF$  are roughly independent of the passivation layer thickness (see Fig. 3). The unpassivated sample in Fig. 5 has a higher  $EQE$  between 500 and 750 nm compared to all passivated 15pre-DT samples, resulting in a high  $J_{SC}$ . For those samples, there is a clear trend towards higher  $EQEs$  in the long wave length region for thicker passivation layers. Therefore, the  $J_{SC}$  of the 15pre-DT10 sample is lowest compared to all other 15pre-DT samples and it increases monotonously with passivation layer thickness, so that the 15pre-DT70 sample delivers even a slightly higher  $J_{SC}$  than the unpassivated 15preDT0 sample. The efficiency follows the trend of the  $J_{SC}$ , with a drop from the 15Pre-DT0 to the 15-PreDT10 sample, and an increase in efficiency for thicker passivation layers. However, none of the passivated samples is more efficient than the unpassivated one. Even for the 7.5preDT samples (not presented in a figure) the  $EQE$  in the long wavelength region is higher for the 7.5preDT50 sample compared to the 7.5preDT20 sample. When re-measuring the  $JV$  curves at 300 K during the  $JVT$  measurement sweep, the 7.5Pre-DT50 sample had degraded during 44 days of storage at room temperature and in air. The  $V_{OC}$  at 300 K was  $\sim 50 \text{ meV}$  lower than previously measured and the  $JV$



**Fig. 3.** Average open-circuit voltage  $V_{OC}$ , short-circuit current density  $J_{SC}$ , fill factor and efficiency for all sample types. The error bars indicate the standard deviation sigma, which is in most cases smaller than the marker and thus not visible. The light intensity was calibrated with a Si solar cell to obtain a photon flux corresponding to  $1000 \text{ W/m}^2$  at AM 1.5. Post-DT samples were treated with an in-situ post-deposition treatment just after CIGS evaporation. On 15Pre-DT and 7.5Pre-DT a 15 respectively 7.5 nm NaF precursor layer was evaporated on the samples just before the CIGS co-evaporation. On the barrier samples an alkali diffusion barrier was deposited directly onto the glass.



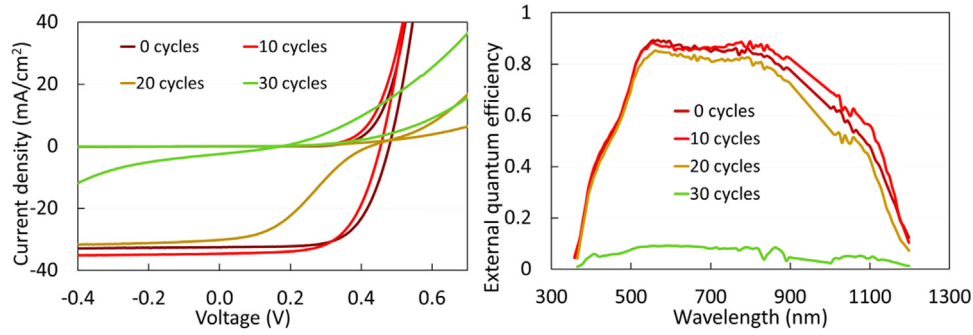


**Fig. 4.** Current-voltage (*JV*) curves (left) in the dark and under illumination and external quantum efficiency (*EQE*) (right) for selected post-deposition treated (post-DT) samples. Due to measurement artifacts, the data in the region between 900 and 1000 nm has been interpolated.

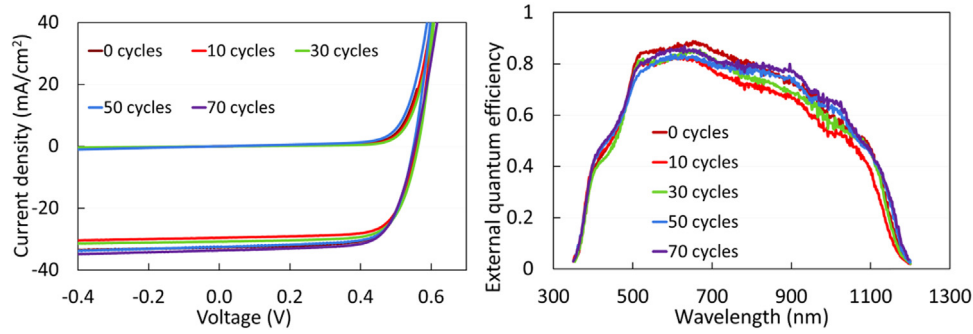


**Fig. 5.** Current-voltage (*JV*) curves (left) in the dark and under illumination and external quantum efficiency (*EQE*) (right) for selected samples with a 15 nm NaF precursor layer (15PreDT samples).

curve has a kink and roll-over.

The barrier samples with passivation layer block the current similarly as the post-DT samples (Fig. 3 and Fig. 6). The major difference from the post-DT samples is an expected lower  $V_{OC}$  for all samples due to a lack of Na (see for example [32] and references therein). The *EQE* of the barrier20 sample is lowered independently of the wavelength, which indicated the presence of a barrier for the photocurrent. The photocurrent is also lowered in the corresponding *JV* curve.

#### 4.2. CV measurements

In order to separate the effects of sodium induced changes in the doping concentration from the passivation effect on the *JV* and *EQE*, CV measurements were conducted. The average doping concentration of various samples can be found in Fig. 7. As expected, the barrier samples have the lowest net acceptor concentration ( $\sim 10^{15} \text{ cm}^{-3}$ ). The baseline sample and the 7.5pre-DT samples have similar doping densities ( $10^{16} - 10^{17} \text{ cm}^{-3}$ ). The highest acceptor concentration is measured on the 15preDT and the post-DT samples.

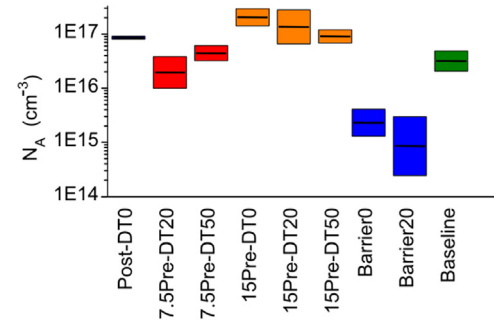


**Fig. 7.** Net acceptor concentration  $N_A$  calculated from current-voltage (CV) measurements on 4 cells per sample. The boxes indicate the standard deviation. The sample names are explained in Table 1.

#### 4.3. JVT measurements

As mentioned in the introduction, the data from *JVT* measurements can help to illuminate the physics at the rear contact. First, we examine which model we can use, then we describe the bending of the  $V_{OC}-T$

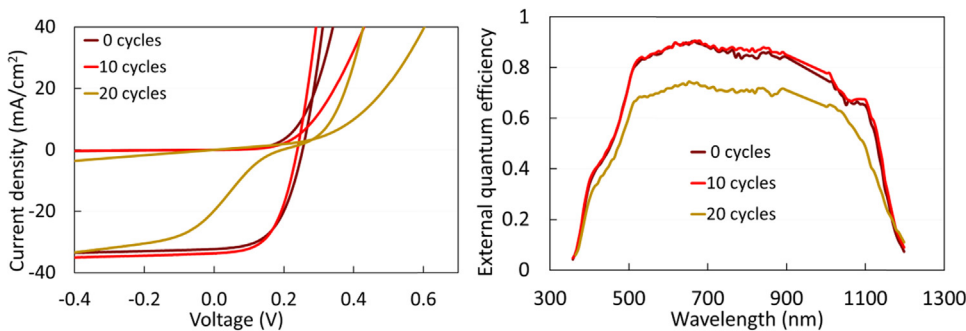


**Fig. 6.** Current-voltage *JV* curves (left) in the dark and under illumination and external quantum efficiency *EQE* (right) for the barrier samples, i.e. the samples with an alkali diffusion barrier deposited directly on the cleaned glass. Due to measurement artifacts, the measurement data in the region between 900 and 1000 nm has been interpolated.

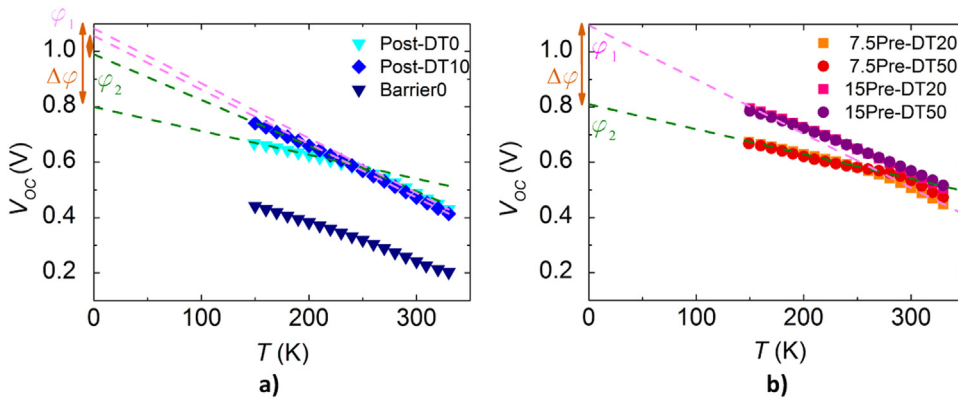


**Fig. 8.** Open-circuit voltage-temperature ( $V_{OC}$ - $T$ ) graphs for the temperature dependent current-voltage ( $JVT$ ) measurements on a) the post-DT0, the post-DT10 and the barrier0 sample and b) the pre-DT20 and pre-DT50 sample. In graph a) the extrapolations towards 0 K at low (150–180 K) and high temperatures (300–330 K) are illustrated for post-DT samples and the values  $\phi_1$ ,  $\phi_2$  and  $\Delta\phi$  are marked on the  $V_{OC}$ -axis. In graph b) the extrapolation of graphs at low and high temperatures is exemplified for the 7.5pre-DT20 sample. In both cases the green lines mark the extrapolation at low temperatures and magenta lines the extrapolation at high temperatures. The sample names are explained in Table 1.

curves (Fig. 8) of different samples qualitatively and finally we quantify the differences in bending with the help of a parameter  $\Delta\phi$ , which is also a measure of  $\phi_b$  (see the Supplementary information in the Appendix).

For 100% photon flux and regardless of the measurement temperature, none of the  $JV$  curves has any roll-over, with exception of the post-DT sample's  $JV$  curve which has a slight roll-over at low temperatures. As  $J_{ob}$  depends exponentially on the temperature (see theory section and appendix), it is negligibly small at low temperatures and  $G_b$  must be large to explain the lack of a roll-over. Apart from the degraded 7.5pre-DT50 sample, no kinks are visible in the  $JV$  curves at 100% photon flux. The  $V_{OC}$  we measured for small light fluxes is always lower than the  $V_{OC}$  for larger light fluxes at the same temperature – in agreement with the super-position principle [26] and the calculations for model 1 presented in the theory section but in disagreement with the phototransistor model (model 2) as presented in [13] and discussed in the appendix. Therefore model 2 can be excluded and model 1 from the theory section and the appendix will be used.

In Fig. 8 the  $V_{OC}$  for the samples is plotted over the temperature. Two categories of samples can be discerned concerning the bending of the  $JV$  curve: The  $JV$  curves of the unpassivated post-DT sample, the barrier sample and the two 15pre-DT samples bend only slightly towards lower  $V_{OC}$  for decreasing temperatures. Contrary, the  $JV$  curves of the post-DT10 and the 7.5pre-DT samples bend strongly towards a much lower  $V_{OC}$  at decreasing temperatures.

To extract a measure for this difference in the graphs' curvature, the  $V_{OC}$ - $T$  graphs were fitted by one linear fit through the four data points at the highest temperatures (300–330 K) and one linear fit through the four data points at the lowest measurement temperatures (150–180 K) (see Fig. 8). For both linear fits the  $V_{OC}$  at  $T = 0$  K was extrapolated, giving a value  $\phi_1$  for the high temperature fit and  $\phi_2$  for the low temperature fit.  $\phi_1$ ,  $\phi_2$  and the difference  $\Delta\phi$  are summarized in Table 2.

Except for the barrier sample,  $\phi_1$  lies between 1.07 and 1.14 V for all samples and is somewhat higher than the band gap extracted from EQE

measurements of 1.06 eV and thus  $\Delta\phi$  is a measure for  $\phi_b$ . If the conditions  $J_{ob} > J_{ib}$  and  $J_{ob} > G_b V_{OCb}$ , (compare appendix) were not fulfilled at high temperatures,  $\phi_1$  would extrapolate to a lower value than the band gap.  $\phi_1$  is neither impacted by the Na supply method nor the existence or the thickness of a passivation layer. For the barrier sample  $\phi_1$  is only 0.66 eV. Without a deeper analysis of the temperature dependence of the (main) diode's ideality factor, we can conclude that the recombination for the sample with a diffusion barrier takes place at the front contact interface and differs from the rest of the samples [33]. For this sample  $\Delta\phi \neq \phi_b$ .

The TEM results from the 7.5pre-DT70 and post-DT50 sample are presented Fig. 9. For the sample 7.5pre-DT70, the presence of the oxide layer can be seen in the Bright Field (BF) image (Fig. 9A) and also in the consecutive RGB and RB reconstructed images (Red=In / Green=O / Blue=Mo). From the RGB image we note discontinuities in the O signal, and from the RB image a smooth transition from Mo to In with no clear gap in between. The line profiles integrated over a weak O area show a low amount of O at the interface, but also no obvious separation between the Cu/In/Ga and the Mo interfaces. We also note an accumulation of Ga correlating with the presence of O. If the line profile is integrated over a non-deteriorated area (i.e. where O signal is manifest), the result is fairly comparable to the profiles shown to the right for the post-DT50 sample. Using EELS maps acquired at higher energy-loss (not shown here) we measured an Al signal correlated with the oxygen location.

For the post-DT50 sample the oxide layer is also visible in the BF and the RGB images in Fig. 9 B. The RB image reveals in this case a clear gap separating the In from the Mo, and the integrated line profiles at the bottom of the same figure show clear signals from O and Ga filling the gap between the Mo back contact and the CIGS absorber layer.

## 5. Discussion

### 5.1. $JV$ measurements and TEM

All distorted  $JV$  curves measured at 300 K have both a roll-over and a kink (see Fig. 4 and Fig. 6 and the introduction). Generally, a kink in  $JV$  curves indicates that hole extraction from the CIGS layer into the rear contact is hindered [10]. A high differential resistance (roll-over) for voltages above  $V_{OC}$  indicates that hole injection from the contact into the CIGS layer is reduced [8,10,12]. As all samples of the same type have been fabricated during a short period of time with identical process recipes (and in most cases even in the same run batch) and vary only concerning the presence and thickness of the passivation layer, these distortions in the  $JV$  curve stem probably only from this variation. Therefore, we conclude that hole injection and hole extraction are impeded by the energy barrier of the  $Al_2O_3$ .

The observation that the current is blocked by  $Al_2O_3$  layers deposited by more than 20 ALD cycles ( $\sim 1.8$  nm) agrees well with previously measured  $JV$  curves for a Mo- $Al_2O_3$  stack [24], for CIGS solar

**Table 2**

Parameters  $\phi_1$  and  $\phi_2$  and their difference  $\Delta\phi$ , which were extracted from the open-circuit voltage-temperature ( $V_{OC}$ - $T$ ) graph in Fig. 8 at low temperatures and high temperatures respectively.  $\Delta\phi$  is a measure for the bending of the  $V_{OC}$ - $T$  curves and a measure for the barrier at the rear contact  $\phi_b$ , if  $\phi_1$  corresponds to the band gap. Sample names are explained in Table 1.

| Sample name | $\phi_1$ in V | $\phi_2$ in V | $\Delta\phi$ in V |
|-------------|---------------|---------------|-------------------|
| Post-DT0    | 1.1           | 0.8           | 0.3               |
| Post-DT10   | 1.1           | 1.0           | 0.1               |
| 7.5Pre-DT20 | 1.1           | 0.8           | 0.3               |
| 7.5Pre-DT50 | 1.1           | 0.8           | 0.4               |
| 15Pre-DT20  | 1.1           | 1.0           | 0.1               |
| 15Pre-DT50  | 1.1           | 0.9           | 0.1               |
| Barrier0    | 0.7           | 0.6           | 0.1               |

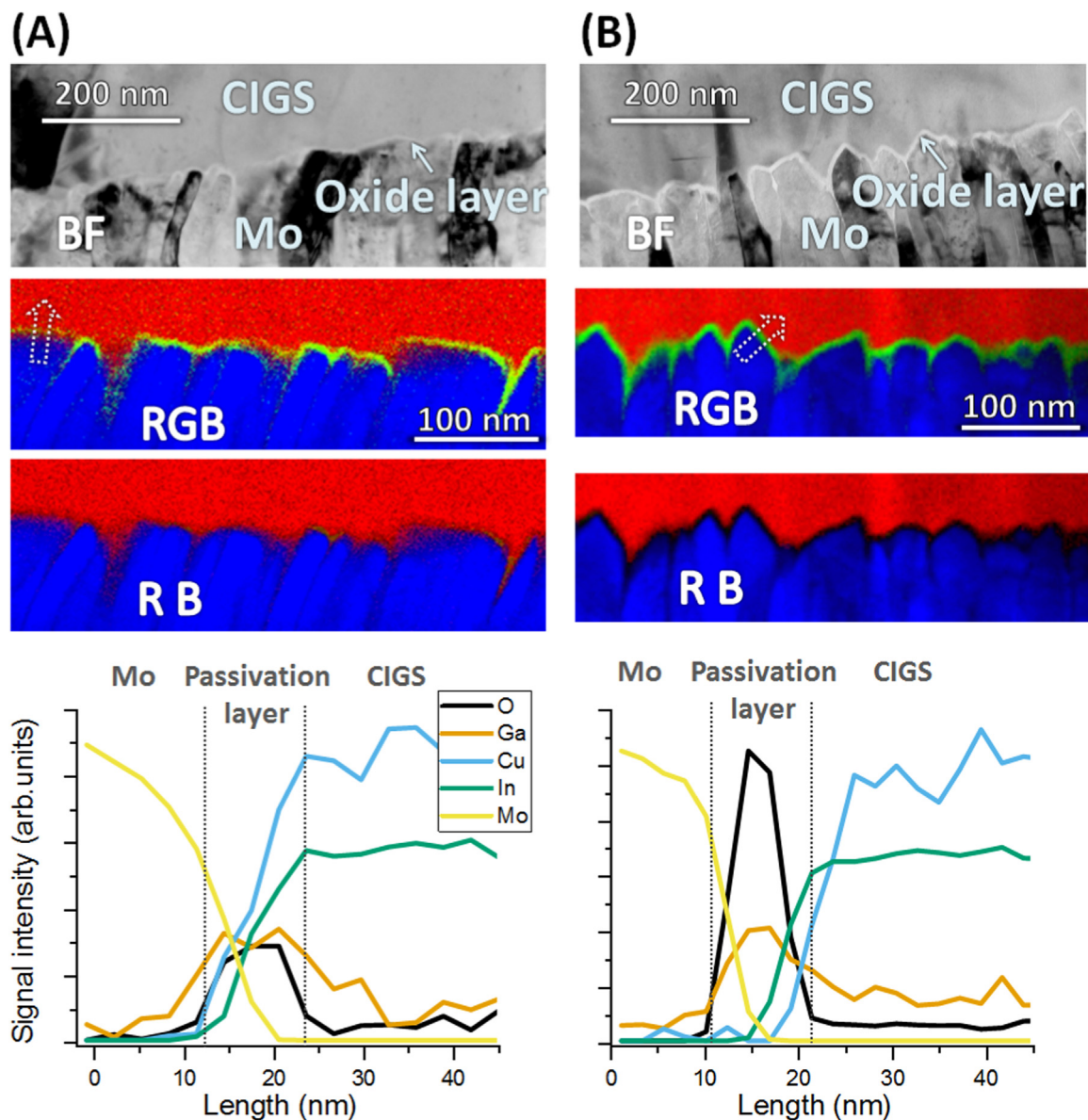


**Fig. 9.** TEM analysis of the samples (A) 7.5pre-DT70 and (B) post-DT50, showing for both the Bright Field image (BF), the red-green-blue (RGB) and the red-blue (RB) reconstructed images (with Red: In – Green: O – Blue: Mo), and the EELS intensity profiles of O, Ga, Cu, In and Mo as integrated over the area symbolized by the white dotted arrows in the RGB maps. In the EELS intensity profile the length of the x-axes corresponds to the length of the arrows in the RGB images and the x-axes' origin is placed at 0 nm. The aluminum signal correlates with oxygen but cannot be extracted from this data-set due to the used energy range.

cells with an  $\text{Al}_2\text{O}_3$  passivation layer at the front contact [34] and CIGS solar cells with a passivation layer at the rear contact without extra Na supply [3]. Vermang et al. [3] measured similarly blocking *JV* curves on their samples, which were passivated with a < 5 nm thick  $\text{Al}_2\text{O}_3$  passivation layer from the same ALD process without contact openings and were produced on soda-lime glass and without extra Na supply. They concluded that their measured *JV* curves disprove a sufficient contact through the passivation layer and indicate that the passivation layer is intact. For samples with a front contact passivation a thickness of about 1 nm was found to be the maximum thickness that still allows for high tunneling currents and negligible transport losses [34]. The series resistance increased significantly for 1.7 nm thick passivation layers compared to a reference sample. For a 2.2 nm thick passivation layer a kink and roll-over was measured in the light *JV* curve. In agreement with these references, we conclude that the passivation layer for the post-deposition samples are completely covering after CIGS processing for more than 20 ALD cycles, i.e. 1.8 nm.

The current flow through passivation layers deposited by up to 20

ALD cycles can be either explained by a hole tunneling current through the passivation layer as in [34] or by a hole current directly from the CIGS into the Mo (possibly through  $\text{MoSe}_2$ ), if the  $\text{Al}_2\text{O}_3$  layer does not completely cover the Mo layer. We will use the data from the *JVT* measurements to get further insight into this question.

As the *JV* curves of pre-DT samples are not visibly distorted by the  $\text{Al}_2\text{O}_3$  layer for at least up to 70 ALD cycles (see Fig. 5), the hypothesis that intentionally patterned  $\text{Al}_2\text{O}_3$  passivation layers conduct current only via the nano-point contacts needs to be reconsidered. Especially,  $\text{Al}_2\text{O}_3$  passivation layers, that were deposited by the same ALD process to similar thicknesses, intentionally patterned either by nano-particles [2,3] or electron-beam lithography [4] and had a NaF precursor applied onto them before the CIGS evaporation, probably do not conduct current only through the intentional contacts. On the other hand, post-DT solar cells with 27 nm thick  $\text{Al}_2\text{O}_3$  passivation layers that were patterned by electron-beam lithography with a similar pitch and contact area have been shown to be sufficiently conductive [31].

The substantial difference in rear contact conductivity for different



Na supply methods raises the question about how these methods modify the rear contact region. We propose two hypotheses on how the NaF precursor alters the conductivity through the  $\text{Al}_2\text{O}_3$  layer: 1) It opens up holes in the  $\text{Al}_2\text{O}_3$  and a  $\text{MoSe}_2$  layer is formed between the Mo and CIGS layer, so that the current transport occurs from the CIGS to the Mo via the  $\text{MoSe}_2$  layer. 2) It changes the  $\text{Al}_2\text{O}_3$  chemically and thus its electrical properties.

In [35] X-ray photoelectron spectroscopy (XPS) was used to confirm hypothesis 1.  $\text{MoSe}_2$  is formed in the holes of a locally non-covering passivation layer, whereas no  $\text{MoSe}_2$  is formed on a closed passivation layer. Thus, detecting  $\text{MoSe}_2$  would indicate that the passivation layer is not closed. XPS could however not confirm the existence of  $\text{MoSe}_2$  on samples with a NaF precursor layer on a Mo-coated glass substrate with an  $\text{Al}_2\text{O}_3$  layer, which were annealed in a Se atmosphere and vacuum as a reference. This result neither excludes nor confirms hypothesis 1. A possibility to verify hypothesis 2 is to prove the existence of other Al-compounds than  $\text{Al}_2\text{O}_3$  at the rear contact. However, when comparing annealed glass-Mo- $\text{Al}_2\text{O}_3$  stacks with and without a NaF precursor on top, the existence of an additional chemical shift in the Al signal for the samples with NaF could not be verified. Especially,  $\text{AlF}_3$  signals could not be distinguished from the Al signals. This result neither confirms nor contradicts hypothesis 2.

From the TEM analysis, we confirm a conformal  $\text{Al}_2\text{O}_3$  layer growth but we also identified a fair amount of Ga incorporated into this oxide layer, apparently as GaO. When the NaF was introduced as a precursor layer, the passivation layer deteriorates leading to direct contact between the CIGS absorber layer and the Mo back contact, as reflected by the line profiles in Fig. 9. In such locations we consistently observe a more gradual drop in Mo signal intensity that can indicate the underlying formation of  $\text{MoSe}_2$ . The use of a NaF-PDT preventing the direct contact between the NaF and the  $\text{Al}_2\text{O}_3$  seems to preserve the oxide layer integrity, but does not prevent the formation of GaO. Therefore, and despite the substantial 6.3 nm  $\text{Al}_2\text{O}_3$  layer, a direct contact between the CIGS and the Mo seems to occur for the 7.5pre-DT70 sample, but not for the post-DT50 one.

## 5.2. EQE measurements

In Figs. 4 and 5, EQE at long wavelengths increases for thicker  $\text{Al}_2\text{O}_3$  layers. Four effects can be responsible for these differences: doping effects, differences in minority carrier diffusion length, optical effects or passivation effects. For photons with long wavelengths free electrons are created closer to the rear contact. Thus, the collection probability for these free electrons is sensitive to the recombination at the rear contact and a short diffusion length. If the acceptor concentration is low, the space charge region reaches further back into the CIGS layer and the influence of the rear contact recombination and short diffusion length on the collection probability is counteracted by the electrical field in the space charge region. This mechanism explains the difference between the very high EQEs for long wavelengths for the samples with a diffusion barrier, which have lower acceptor concentrations according to the CV measurements, and the low EQEs for long wavelengths 15pre-DT samples, which have a higher acceptor concentration. Therefore, the EQEs should be only compared for samples with similar apparent doping from Fig. 7.

Optical effects leading to differences in the EQE may stem from a higher reflectance at passivated rear contacts [4,31] compared to the unpassivated ones. In that case higher reflection at the rear contact enhances especially the absorption of photons with long wavelengths, as photons with short wavelengths have a high absorption coefficient and are mostly already absorbed before they reach the rear contact. But despite that the rear reflectance increases with increasing  $\text{Al}_2\text{O}_3$  thickness, earlier SCAPS and optical simulations [4,31] and electrical modelling [31] comparing unpassivated reference samples with samples coated with a 300 cycle  $\text{Al}_2\text{O}_3$  layer (4 times the thickness used in this study) show that the higher EQE for passivated samples can only

partially (< 10%) be explained by the higher reflection at the passivated contact. Thus, within a sample type (compare Fig. 1 and Table 1) differences in the EQE stem most probably from a passivation effects leading to reduced back contact recombination.

## 5.3. JVT measurements

For the post-DT samples, a 10 cycle passivation layer lowers  $\Delta\phi$  by 0.2 eV compared to the (unpassivated) post-DT0 sample. If we assume that the  $\text{Al}_2\text{O}_3$  layer is completely covering for post-DT samples, the hole current needs to tunnel through the  $\text{Al}_2\text{O}_3$  layer and pass the rear interface region of the CIGS absorber where the electrical field effect stemming from the negative charges in the passivation layer [7] reduces the band bending and thus  $\phi_b$ . As long as the passivation layer is so thin, that the holes can tunnel through it, the energy off-set at the passivation layer is not visible in the JVT measurements, but the reduced band bending due to the negative oxide charge in the  $\text{Al}_2\text{O}_3$  is. On the other hand, if sufficiently large conducting holes existed in the passivation layer, the hole current would not be affected by the electrical field. We can thus conclude that the passivation layer on post-DT samples probably completely covers the rear contact and that the current probably tunnels through the layer.

If we assume that there are holes in the  $\text{Al}_2\text{O}_3$  layer for the pre-DT samples (hypothesis1), the measured  $\Delta\phi$  is an estimate of  $\phi_b$  at the CIGS-MoSe<sub>2</sub> interface. If the holes were large enough, the band bending at the CIGS-MoSe<sub>2</sub> interface would not be affected by the field effect and  $\phi_b$  would not depend on the thickness of a passivation layer. Indeed, our results do not show any correlation between  $\Delta\phi$  and the passivation layer thickness. Contact resistance,  $\phi_b$  and the likelihood for a roll-over in a temperature range between 100 and 300 K decreases for higher Na concentrations at CIGS-MoSe<sub>2</sub> interfaces according to the literature [19,22].  $\Delta\phi$  is indeed 0.2 eV lower for the 15preDT20 and the 15preDT50 sample compared to the 7.5PreDT20 (and 0.3 eV lower compared to the 7.5PreDT50 sample, which had however - as mentioned in the results section - degraded). In summary, our results do not contradict hypothesis 1.

The current blocking for the post-DT samples with more than 2 nm thick  $\text{Al}_2\text{O}_3$  layers, indicate that the direct tunneling of holes can be excluded for these  $\text{Al}_2\text{O}_3$  layers and that the energy barrier associated with the  $\text{Al}_2\text{O}_3$  layer is too large to be overcome. According to hypothesis 2 then, Na or F doping lowers this barrier. For example, it has been shown that oxygen vacancies  $V_O$  in  $\text{AlO}_x$  can form a defect band close to the band gap, which acts as a “conduction band” [36]. Doping can also introduce traps that increase the likelihood for Frenkel-Poole emission, which is a conduction-limited and trap-assisted carrier transport mechanism [37]. However, the JVT measurements probe the largest energy barrier in the valence band at the rear contact, and cannot per-se distinguish the energy barrier associated with the  $\text{Al}_2\text{O}_3$  layer from the one associated with the band bending in the CIGS. If Na or F doping reduces the former below the latter, the latter will be detected and changes in barrier height will be changes in band bending. Yoon et al. [22] proposed that Na directly reduces the barrier height at the CIGS-MoSe<sub>2</sub> interface by increasing the carrier concentration in the CIGS or MoSe<sub>2</sub>, and not indirectly by enhancing the formation of MoSe<sub>2</sub>. Even this effect can explain our results. Thus, the JVT measurement, cannot distinguish between the two hypotheses, conduction through holes in the passivation layer or conduction due to a change of the electrical properties of the passivation layer.

## 6. Conclusion

For NaF post-DT samples and samples with an alkaline diffusion barrier between the glass and the Mo film, a good contact between the CIGS and the Mo layer – probably a tunneling contact - can be established for very thin  $\text{Al}_2\text{O}_3$  passivation layers of about 1 nm. Although these thin layers increase the  $J_{SC}$ , they do not increase the solar cell



efficiency either due to a lower  $FF$  and/or due to a lower  $V_{OC}$ . The 1 nm thick passivation layer decreases the energy barrier for holes at the rear contact compared to the unpassivated case, probably as a negative oxide charge reduces the band bending in the CIGS. For even thicker  $Al_2O_3$  layers, the current is blocked and therefore the efficiency is not enhanced for any passivation layer thickness. In contrast, for samples with NaF pre-deposition treatment and up to about 6.3 nm (70 cycles) thick  $Al_2O_3$  layers, the NaF precursor increases the conductivity through the passivation layer so that the current is not blocked. Although the efficiency of these passivated solar cells does not exceed the efficiency of the unpassivated reference, an increase in the  $EQE$  in long wave region for thicker  $Al_2O_3$  layers probably indicates a passivation effect. The TEM analysis of a sample that was pre-deposition treated with NaF reveals a passivation layer degradation leading to a direct contact between the CIGS absorber layer and the Mo back contact and maybe a subsequent formation of  $MoSe_2$ . For pre-deposition treated samples, an analysis of the dependence of the open circuit voltage on temperature indicates that a thicker NaF precursor layer lowers the height of the hole barrier at the rear contact. In conclusion, using thin  $Al_2O_3$  layers and a NaF pre-deposition treatment may be a cost-effective way of creating nano-openings in a rear-contact passivation layer without the need of patterning the passivation layer for contacting in an extra fabrication step.

## Acknowledgements

The authors thank Carl Hägglund for determining the thickness of the  $Al_2O_3$  layers by ellipsometry measurements.

## Funding sources

This work was supported by the Swedish Science Council via grant 43523-1 and StandUp for Energy as well as the EU-funded project ARCIGS-M.

## Conflict of interest

The authors declare that there is no conflict of interest regarding the publication of this article.

## Appendix A. Supplementary material

The method of extracting the hole barrier height at the rear contact from  $JVT$  measurements is explained and derived in the online version at [doi:10.1016/j.solmat.2018.07.017](https://doi.org/10.1016/j.solmat.2018.07.017). Even assumptions and limitations of the method are outlined there.

## References

- [1] M.A. Green, K. Emery, Y. Hishikawa, W. Warta, Solar cell efficiency tables, *Prog. Photovolt. Res. Appl.* 24 (2016) 905–913, <https://doi.org/10.1002/pip.2788>.
- [2] B. Vermang, J.T. Wätjen, C. Frisk, V. Fjällström, F. Rostvall, M. Edoff, P. Salome, J. Borme, N. Nicoara, S. Sadewasser, Introduction of Si PERC rear contacting design to boost efficiency of  $Cu(In,Ga)Se_2$  solar cells, *IEEE J. Photovolt.* 4 (2014) 1644–1649, <https://doi.org/10.1109/JPHOTOV.2014.2350696>.
- [3] B. Vermang, V. Fjällström, X. Gao, M. Edoff, Improved rear surface passivation of  $Cu(In,Ga)Se_2$  solar cells: a combination of an  $Al_2O_3$  rear surface passivation layer and nanosized local rear point contacts, *IEEE J. Photovolt.* 4 (2014) 486–492, <https://doi.org/10.1109/JPHOTOV.2013.2287769>.
- [4] B. Vermang, J.T. Wätjen, V. Fjällström, F. Rostvall, M. Edoff, R. Gunnarsson, I. Pilch, U. Helmersson, R. Kotipalli, F. Henry, D. Flandre, Highly reflective rear surface passivation design for ultra-thin  $Cu(In,Ga)Se_2$  solar cells, *Thin Solid Films* 582 (2014) 300–303, <https://doi.org/10.1016/j.tsf.2014.10.050>.
- [5] W.-W. Hsu, J.Y. Chen, T.-H. Cheng, S.C. Lu, W.-S. Ho, Y.-Y. Chen, Y.-J. Chien, C.W. Liu, Surface passivation of  $Cu(In,Ga)Se_2$  using atomic layer deposited  $Al_2O_3$ , *Appl. Phys. Lett.* 100 (2012) 23508, <https://doi.org/10.1063/1.3675849>.
- [6] R. Kotipalli, B. Vermang, J. Joel, R. Rajkumar, M. Edoff, D. Flandre, Investigating the electronic properties of  $Al_2O_3/Cu(In,Ga)Se_2$  interface, *AIP Adv.* 5 (2015) 107101, <https://doi.org/10.1063/1.4932512>.
- [7] J.R. Weber, A. Janotti, C.G. Van de Walle, Native defects in  $Al_2O_3$  and their impact on III-V/ $Al_2O_3$  metal-oxide-semiconductor-based devices, *J. Appl. Phys.* 109 (2011) 33715, <https://doi.org/10.1063/1.3544310>.
- [8] S. Puttnins, M.S. Hammer, J. Neerken, I. Riedel, F. Daume, A. Rahm, A. Braun, M. Grundmann, T. Unold, Impact of sodium on the device characteristics of low temperature-deposited  $Cu(In,Ga)Se_2$  solar cells, *Thin Solid Films* 582 (2015) 85–90, <https://doi.org/10.1016/j.tsf.2014.07.048>.
- [9] F. Pianezzi, P. Reinhard, A. Chirilă, B. Bissig, S. Nishiwaki, S. Buecheler, A.N. Tiwari, Unveiling the effects of post-deposition treatment with different alkaline elements on the electronic properties of CIGS thin film solar cells, *Phys. Chem. Chem. Phys.* 16 (2014) 8843–8851, <https://doi.org/10.1039/c4cp00614c>.
- [10] M. Richter, C. Schubert, P. Eraerds, J. Parisi, I. Riedel, T. Dalibor, J. Palm, Comprehensive simulation model for  $Cu(In,Ga)(Se,S)_2$  solar cells, *Sol. Energy Mater. Sol. Cells* 132 (2015) 162–171, <https://doi.org/10.1016/j.solmat.2014.08.047>.
- [11] S.H. Demtsu, J.R. Sites, Effect of back-contact barrier on thin-film CdTe solar cells, *Thin Solid Films* 510 (2006) 320–324, <https://doi.org/10.1016/j.tsf.2006.01.004>.
- [12] N. Neugebohrn, M.S. Hammer, J. Neerken, J. Parisi, I. Riedel, Analysis of the back contact properties of  $Cu(In,Ga)Se_2$  solar cells employing the thermionic emission model, *Thin Solid Films* 582 (2015) 332–335, <https://doi.org/10.1016/j.tsf.2014.10.073>.
- [13] T. Ott, F. Schönberger, T. Walter, D. Hariskos, O. Kiowski, O. Salomon, R. Schöffler, Verification of phototransistor model for  $Cu(In,Ga)Se_2$  solar, *Thin Solid Films* 582 (2015) 392–396, <https://doi.org/10.1016/j.tsf.2014.09.025>.
- [14] T. Ott, T. Walter, D. Hariskos, Accelerated aging and contact degradation of CIGS solar cells, *IEEE J. Photovolt.* 3 (2013) 514–519 (10.1109/PVSC-Vol2.2013.6656770).
- [15] A. Rockett, J.K.J. van Duren, A. Pudov, W.N. Shafarman, First quadrant phototransistor behavior in  $CuInSe_2$  photovoltaics, *Sol. Energy Mater. Sol. Cells* 118 (2013) 141–148, <https://doi.org/10.1016/j.solmat.2013.07.032>.
- [16] G.T. Koishiyevev, J.R. Sites, Determination of back contact barrier height in  $Cu(In,Ga)(Se,S)_2$  and CdTe solar cells, in: Conference Rec. 33rd Photovolt. Spec. Conference San Diego, CA, USA: 2008. pp. 1–3. doi: 10.1109/PVSC.2008.4922886.
- [17] K.-J. Hsiao, J.-D. Liu, H.-H. Hsieh, T.-S. Jiang, Electrical impact of  $MoSe_2$  on CIGS thin-film solar cells, *Phys. Chem. Chem. Phys.* 15 (2013) 18174–18178, <https://doi.org/10.1039/c3cp53310g>.
- [18] A. Niemegeers, M. Burgelman, Effects of the Au/CdTe back contact on IV and CV characteristics of Au/CdTe/CdS/TCO solar cells, *J. Appl. Phys.* 81 (1997) 2881, <https://doi.org/10.1063/1.363946>.
- [19] R. Caballero, M. Nichterwitz, A. Steigert, A. Eicke, I. Lauermann, H.W. Schock, C.A. Kaufmann, Impact of Na on  $MoSe_2$  formation at the CIGSe/Mo interface in thin-film solar cells on polyimide foil at low process temperatures, *Acta Mater.* 63 (2014) 54–62, <https://doi.org/10.1016/j.actamat.2013.09.051>.
- [20] T. Wada, N. Kohara, S. Nishiwaki, T. Negami, Characterization of the  $Cu(In,Ga)Se_2/Mo$  interface in CIGS solar cells, *Thin Solid Films* 387 (2001) 118–122, [https://doi.org/10.1016/S0040-6090\(00\)01846-0](https://doi.org/10.1016/S0040-6090(00)01846-0).
- [21] N. Kohara, S. Nishiwaki, Y. Hashimoto, T. Negami, T. Wada, Electrical properties of the  $Cu(In,Ga)Se_2/MoSe_2/Mo$  structure, *Sol. Energy Mater. Sol. Cells* 67 (2001) 209–215, [https://doi.org/10.1016/S0927-0248\(00\)00283-X](https://doi.org/10.1016/S0927-0248(00)00283-X).
- [22] J. Yoon, J. Kim, W. Kim, J. Park, Y. Baik, T. Seong, J. Jeong, Electrical properties of CIGS/Mo junctions as a function of  $MoSe_2$  orientation and Na doping, *Prog. Photovolt. Res. Appl.* 22 (2014) 90–96, <https://doi.org/10.1002/pip.21002>.
- [23] E. Jarzemowski, F. Syrowatka, K. Kaufmann, W. Fränzel, T. Hölscher, R. Scheer, The influence of sodium on the molybdenum/ $Cu(In,Ga)Se_2$  interface recombination velocity, determined by time resolved photoluminescence, *Appl. Phys. Lett.* 107 (2015) 51601, <https://doi.org/10.1063/1.4928187>.
- [24] M.D. Groner, J.W. Elam, F.H. Fabreguette, S.M. George, Electrical characterization of thin  $Al_2O_3$  films grown by atomic layer deposition on silicon and various metal substrates, *Thin Solid Films* 413 (2002) 186–197, [https://doi.org/10.1016/S0040-6090\(02\)00438-8](https://doi.org/10.1016/S0040-6090(02)00438-8).
- [25] J. Lindahl, U. Zimmermann, P. Szaniawski, T. Törndahl, A. Hultqvist, P. Salome, C. Platzter-Björkman, M. Edoff, Inline  $Cu(In,Ga)Se_2$  co-evaporation for high-efficiency solar cells and modules, *IEEE J. Photovolt.* 3 (2013) 1100–1105 (10.1109/JPHOTOV.2013.2256232).
- [26] R. Scheer, H.-W. Schock, Chalcogenide Photovoltaics: Physics, Technologies, and Thin Film Devices, Wiley-Vch Verlag GmbH & Co, KGaA, 2011.
- [27] R.M. Langford, M. Rogers, In situ lift-out: steps to improve yield and a comparison with other FIB TEM sample preparation techniques, *Micron* 39 (2008) 1325–1330, <https://doi.org/10.1016/j.micron.2008.02.006>.
- [28] T. Eisenbarth, R. Caballero, M. Nichterwitz, C.A. Kaufmann, H.-W. Schock, T. Unold, Characterization of metastabilities in  $Cu(In,Ga)Se_2$  thin-film solar cells by capacitance and current-voltage spectroscopy, *J. Appl. Phys.* 110 (2011) 94506, <https://doi.org/10.1063/1.3656453>.
- [29] T. Eisenbarth, T. Unold, R. Caballero, C.A. Kaufmann, H.-W. Schock, Interpretation of admittance, capacitance-voltage, and current-voltage signatures in  $Cu(In,Ga)Se_2$  thin film solar cells, *J. Appl. Phys.* 107 (2010) 34509, <https://doi.org/10.1063/1.3277043>.
- [30] M. Roy, S. Damaskinos, J.E. Phillips, The diode current mechanism in  $CuInSe_2/(CdZn)S$  heterojunctions, in: Conference Rec. 20th. IEEE Photovolt. Spec. Conference Las Vegas, NV, USA: pp 1618–1623. doi: 10.1109/PVSC.1988.105986, 1988.
- [31] D. Ledinek, P. Salome, C. Hägglund, U. Zimmermann, M. Edoff, Rear contact passivation for high band gap  $Cu(In,Ga)Se_2$  solar cells with a flat Ga profile, *IEEE J. Photovolt.* (2018), <https://doi.org/10.1109/JPHOTOV.2018.2813259>.
- [32] A. Urbaniak, M. Igalson, F. Pianezzi, S. Bücheler, A. Chirilă, P. Reinhard, A.N. Tiwari, Effects of Na incorporation on electrical properties of  $Cu(In,Ga)Se_2$ -based photovoltaic devices on polyimide substrates, *Sol. Energy Mater. Sol. Cells* 128 (2014) 52–56, <https://doi.org/10.1016/j.solmat.2014.05.009>.

- [33] R. Scheer, Activation energy of heterojunction diode currents in the limit of interface recombination, *J. Appl. Phys.* 105 (2009) 104505, <https://doi.org/10.1063/1.3126523>.
- [34] J. Keller, F. Gustavsson, L. Stolt, M. Edoff, T. Törndahl, On the beneficial effect of  $\text{Al}_2\text{O}_3$  front contact passivation in  $\text{Cu}(\text{In,Ga})\text{Se}_2$  solar cells, *Sol. Energy Mater. Sol. Cells* 159 (2017) 189–196, <https://doi.org/10.1016/j.solmat.2016.09.019>.
- [35] B.J. Palmer, Improved Rear Surface Passivation of  $\text{Cu}(\text{In,Ga})\text{Se}_2$  Solar Cells: A Combination of an  $\text{Al}_2\text{O}_3$  Rear Surface Passivation Layer and Nanosized Local Rear Point Contacts, Master thesis, Uppsala, 2017.
- [36] S. Nigo, M. Kubota, Y. Harada, T. Hirayama, S. Kato, H. Kitazawa, G. Kido, Conduction band caused by oxygen vacancies in aluminum oxide for resistance random access memory, *J. Appl. Phys.* 112 (2012), <https://doi.org/10.1063/1.4745048>.
- [37] C. Jin, H. Lu, Y. Zhang, Y. Zhang, H. Guan, L. Wu, B. Lu, C. Liu, Transport mechanisms of leakage current in  $\text{Al}_2\text{O}_3/\text{InAlAs}$  MOS capacitors, *Solid. State Electron.* 123 (2016) 106–110, <https://doi.org/10.1016/j.sse.2016.06.006>.